Variable Field Analytical Ultracentrifugation: II. Gravitational Sweep Sedimentation Velocity

Jia Ma[1], Huaying Zhao[1], Julia Sandmaier[2], J. Alexander Liddle[2], Peter Schuck[1]*

[1]*Dynamics of Macromolecular Assembly Section, Laboratory of Cellular Imaging and Macromolecular Biophysics, National Institute of Biomedical Imaging and Bioengineering, National Institutes of Health, Bethesda, MD 20892, United States of America*
[2] *Center for Nanoscale Science and Technology, National Institute of Standards and Technology, Gaithersburg, MD 20899, United States of America*

Running Head: Gravitational Sweep Sedimentation Velocity

*Addresses for correspondence and proofs:
Peter Schuck
National Institutes of Health
Bldg. 13 Rm. 3N17
13 South Drive
Bethesda, Maryland MD 20892
USA

Phone: 301-4351950
Email: schuckp@mail.nih.gov

Abstract

Sedimentation velocity (SV) analytical ultracentrifugation is a classical biophysical technique for the determination of the size-distribution of macromolecules, macromolecular complexes, and nanoparticles. SV has traditionally been carried out at a constant rotor speed, which limits the range of sedimentation coefficients that can be detected in a single experiment. Recently we have introduced tools to implement experiments with variable rotor speeds, in combination with variable field solutions to the Lamm equation, with the application to expedite the approach to sedimentation equilibrium. Here, we describe the use of variable-field sedimentation analysis to increase the size-range of SV experiments by approximately 100-fold through the use of a quasi-continuous increase of rotor speed during the experiment. Such 'gravitational sweep' sedimentation approaches has previously been shown to be very effective in the study of nanoparticles with large size ranges. However, previously diffusion processes were not accounted for, therefore posing a lower limit of particle sizes and limiting the accuracy of the distribution. In the present work, we combine variable field solutions to the Lamm equation with diffusion-deconvoluted sedimentation coefficient distributions $c(s)$, which further extends the macromolecular size-range that can be observed in a single SV experiment while maintaining accuracy and resolution. In this way, approximately five orders of magnitudes of sedimentation coefficients, or eight orders of magnitude of particle mass, can be probed in a single experiment. This can be useful, for example, in the study of proteins forming large assemblies, for example, as in fibrillation process or capsid self-assembly, in studies of the interaction between very dissimilar sized macromolecular species, in the study of broadly distributed nanoparticles.

Keywords: analytical ultracentrifugation; sedimentation velocity; particle size-distribution; nanoparticles

Introduction

The goal of gravitational sweep sedimentation velocity is the detection of all particles in solution over a very large size range by continuously increasing the centrifugal field, causing sequentially smaller particles to sediment. Sedimentation velocity has usually been carried out at constant rotor speed mainly due to the difficulty of solving the Lamm equation – the master equations for sedimentation and diffusion in the centrifugal field – for a time-dependent rotor speed (1). To our knowledge, the consideration of sedimentation in a time-varying centrifugal field was first communicated in the scientific literature 1970 by Nossal & Weiss (1), who presented an approximate analytical Lamm equation solution for sedimentation and diffusion for arbitrary rotor speed profiles, a key element being the transformation of the time variable to a temporal integral over the centrifugal field, which defines an effective sedimentation time. Although the stated purpose was studying sedimentation of small proteins already during the extended rotor acceleration phase to high speeds, and the work was entirely theoretical, the implications of time-varying centrifugal fields went far beyond this.

Shortly after, the first report of experiments systematically exploiting time-variable rotor speeds was for the purpose of characterizing broad particle size distributions of latex suspensions (2). In their comprehensive work, Scholtan & Lange described how the signal from a fixed-radius detector could be transformed directly into a particle size distribution of apparent non-diffusing particles, after corrections for Mie scattering (2). This idea was later termed 'gravitational sweep sedimentation' by Mächtle (3) (and re-stated again in (4)), using a step-wise approximation of an exponential rotor speed profile. With the sedimentation analysis resting on the basis of the time-integral of the centrifugal field, which is a sufficient transformation for non-diffusing particles, this allowed a very wide range of particle sizes to be observed, but it failed in the presence of particles below 10 nm (3).

In the realm of bio-macromolecular applications, the use of three discrete steps of sequentially higher rotor speeds in a single SV run to cover a large particle size range was described by Runge and colleagues in studies on samples of tubulin and neurofilaments (5). Even though not further elaborated, their transformation of signal to apparent sedimentation coefficient distributions $g(s)$ rests, on the relationship mentioned above between the temporal integral of the centrifugal field and migration of non-diffusing particles. This approach was later integrated by Stafford & Braswell as 'wide distribution analysis' into time-derivative analysis (6), and Mach & Arvinte have analogously used a variation of radial-derivate analysis (7) to observe a large range of *s*-values from the analysis of scans acquired in time-varying centrifugal fields.

In the last two decades, modern computational resources and numerical algorithms for differential and integral equations have completely eliminated previous restrictions in considering time-varying centrifugal fields. Our laboratory has originally become interested in time-varying rotor speeds due to the necessity to account for the rotor acceleration phase of the experiment even in conventional constant-speed SV (1, 8). For achieving highest precision in both sedimentation and diffusion, the effective sedimentation time approach (*via* the temporal integral of the centrifugal field) is not optimal. This problem is exacerbated when carrying out experiments with slow rotor acceleration schedules for isothermal centrifugation (9). Therefore, we have incorporated a discretized approximation of the rotor acceleration into the explicit numerical finite element Lamm equation solutions (10–12) used in our SEDFIT software. Recently we have extended the consideration of time-varying rotor speeds from merely modeling the acceleration phase to the modeling of the approach to equilibrium in an arbitrarily changing centrifugal field, with the goal to calculate a rotor speed schedule minimizing the time required to attain sedimentation equilibrium at a target speed (13). While the previous work was in a largely diffusion-dominated regime, in the present work we have focused on the sedimentation-dominated regime to simulate and model sedimentation velocity experiments of particles over a large size-range in time-varying fields. Incorporated as kernel into the well-established diffusion-deconvoluted sedimentation coefficient distributions (14), this allows us to revisit the idea of gravitational sweep sedimentation.

The explicit consideration of diffusion addresses previous limitations and results in an extended size range and hydrodynamic resolution of medium to small particles. To facilitate the experimental application of gravitational sweep SV in practice, we have implemented ancillary tools to prepare centrifugal speed steps schedules for current analytical ultracentrifuges, tools to compensate for field-dependent rotor stretching prior to the data analysis, and tools to reconstruct experimental field profiles from experimental scan data. As a result, freedom in the application of time-varying centrifugal fields over a large range of conditions is achieved for SV analysis. We believe these developments warrant revisiting the idea and practical utility of gravitational sweep sedimentation.

Methods

Theory and Computational

For a simple prediction of the behavior of particles of different size in time-varying centrifugal fields, it is useful to consider the differential of motion of ideal non-diffusing point particles, $r^{(p)}(t)$, which follow

$$\frac{dr^{(p)}}{dt} = s\omega(t)^2 r^{(p)} \tag{1}$$

, where *s* is the sedimentation coefficient, and are therefore exponentially expelled radially with

$$r^{(p)}(t) = m\exp\left[s\int_0^t \omega(t')^2 dt' \right] \tag{2}$$

assuming they are initially located at the meniscus *m* . This is the basis for the approximation of the effective sedimentation time $t^{(\mathrm{sed})}$ that may be attributed to a scan acquired at time *t** at a rotor speed ω*

$$t^{(sed)} = \left(\frac{1}{\omega^*} \right)^2 \int_0^{t^*} \omega(t')^2 dt' \tag{3}$$

such that the Eq. (2) conforms to the conventional expression at constant rotor speed

$$r^{(p)}(t) = m\exp\left[s\omega^{*2}\, t^{(sed)} \right] \tag{4}$$

. This simplification correctly predicts the sedimentation for any $\omega(t)$ but is incorrect for the diffusion process (9). It may be used, however, in the approximation that diffusion is negligible, such as in the *dc/dt* approach to calculate *g*(s*) (6, 15) or in the fixed radius transformation of time to *s*-value applied in (4). In practice, this approach is greatly facilitated by the fact that the Beckman[1] analytical ultracentrifuges used in this study keep track of not only the elapsed time since start of the experiment, but also of $\int \omega^2 dt$ and report this quantity in scan time files. (It should be noted that this quantity is subject to the same experimental time errors in reported scan files as the elapsed time (16, 17).) This eliminates the need to maintain independent record of precise rotor speed schedules (see below).

A more accurate description of the migration in the centrifugal field is achieved when considering both sedimentation and diffusion in the Lamm equation (18)

$$\frac{\partial \chi}{\partial t} = -\frac{1}{r}\frac{\partial}{\partial r}\left(\chi s\omega(t)^2 r^2 - D\frac{\partial \chi}{\partial r} r \right) \tag{5}$$

[1] ***Disclaimer***: Certain commercial equipment, instruments, or materials are identified in order to specify the experimental procedure adequately. Such identification is not intended to imply recommendation or endorsement by the National Institute of Standards and Technology, nor is it intended to imply that the materials or equipment identified are necessarily the best available for the purpose.

where $\chi(r,t)$ denotes the radial and temporal evolution of macromolecular concentration of a species with sedimentation coefficient s and diffusion coefficient D in a sector-shaped solution column rotating with angular velocity $\omega(t)$. The solution of this equation has been implemented in SEDFIT for time-varying fields, in a modification of the finite element algorithm described in (11) where the adaptive radial grid size is eliminated and the grid truncations are carried out only for depleted regions. For species with sedimentation coefficients in excess of 10^{-10} s (1,000 S), this necessitates an increase of the default radial grid size. The time-dependence of the angular velocity $\omega(t)$ was approximated by discretization into 10 sec intervals of constant rotor speed.

The predicted sedimentation profiles are compatible with standard distribution analysis models. Briefly, normalized solutions of Eq. (1) were taken as the kernel of the integral equation

$$a(r,t) \cong \int_{s_{min}}^{s_{max}} \chi_1(r,t,s,D(s))c(s)ds \tag{6}$$

, directly fitted by least-squares to the experimental data $a(r,t)$, to determine the sedimentation coefficient distribution $c(s)$ (14). Due to the consideration of diffusion in the approximation of a scaling law $D(s)$, high-resolution diffusion-deconvoluted sedimentation coefficient distributions $c(s)$ are achieved (14, 19). Following standard techniques for integral equations, Tikhonov or maximum entropy regularization was applied (14, 19). Extension to size-and-shape distributions is seamlessly possible (20) – where sufficient information is present to determine these (21) – as is the incorporation of prior knowledge by Bayesian regularization (22). For the limiting case of very large particles where $D(s) \approx 0$, the $c(s)$ distribution will converge to the apparent sedimentation coefficient distribution ls-$g^*(s)$ (23). Furthermore, the model Eq. (6) can be combined with systematic noise decomposition to account for time-invariant (TI) and radial-invariant (RI) baseline contributions (24, 25).

Prior to analysis *via* Eq. (6), it is important to correct the experimental scans for the rotor-speed dependent rotor stretching. This requires two steps: (1) the translation of the solution column from the detector reference frame to a reference frame at constant meniscus position using a previously measured stretching modulus E, and (2) the compensation of the ensuing changes in the centrifugal field by using an apparent rotor speed (to keep $\omega^2 r$ constant):

$$r' = r - E\omega^2 \quad and \quad \omega' = \omega\sqrt{\frac{r_{mid}}{r_{mid} - E\omega^2}} \tag{7}$$

with r_{mid} denoting the middle of the solution column.

The question arises what choice of $\omega(t)$ would be most desirable. In the absence of other knowledge, when studying potentially extremely broad distributions, it may be reasonable to aim at logarithmically spaced resolution in *s*-values to cover the largest possible range. This can be achieved, for example, when particles transit past the highest observable radius r_{max} with exponentially decreasing *s*-value with time. If Eq. (2) is solved with regard to the *s*-value and an exponential time-course is imposed, it can be shown that this requires a rotor speed profile following a power-law

$$\omega(t) = \omega_{low}\left(\frac{\omega_{max}}{\omega_{low}}\right)^{\frac{(t-t_{low})}{t_{max}-t_{low}}} \tag{8}$$

with ω_{low} and ω_{max} representing lower and upper limits of rotor speed assumed at times t_{low} and t_{max}. Alternatively, another rational choice for the rotor speed schedule would be

$$\omega(t) = \sqrt{\omega_{low}{}^2 + \left(\omega_{max}{}^2 - \omega_{low}{}^2\right)\frac{(t-t_{low})}{t_{max}-t_{low}}} \tag{9}$$

based on the idea of a constant increase in centrifugal field.

A special case for a variable-field sedimentation experiment is sometimes experimentally implemented inadvertently when carrying out the initial adjustment of data acquisition at a rotor speed of 3,000 rpm, prior to acceleration to the target rotor speed of the experiment. This was discouraged in the context of Lamm equation analysis due to the deviations it creates from the default constant rotor acceleration model (26). However, in the framework of variable rotor speed SV this can be naturally accounted for. Even though the scan files do not contain sufficient information to establish and model the speed schedule, with input of the rotor speed ω_{low} (usually 3,000 rpm) it is possible to determine the approximate time the rotor was held at the lower speed from the *t* and $\int\omega^2 dt$ entries of the files, as

$$t_{low} = \left(t - t^{(sed)}\right)\frac{\omega_0^2}{\left(\omega_0^2 - \omega_{low}^2\right)} + \frac{\omega_{low}}{\dot{\omega}} - \frac{2\omega_0^3}{3\dot{\omega}\left(\omega_0^2 - \omega_{low}^2\right)} \tag{10}$$

with $\dot{\omega}$ the constant rotor acceleration (which is not adjustable on current instrumentation) and $t^{(sed)}$ as defined in Eq. (3). SEDFIT has been extended to deduce the presence of an initial low-speed phase from the *t* and $\int\omega^2 dt$ entries of the files, and after user entry of ω_{low}, will create a 'speedsteps.txt' file to accurately model this rotor speed profile.

Similarly, it may be possible to extract the entire history of rotor speed changes from experimental scan data: If at least one scan is available at each rotor speed, then the known fixed rotor acceleration $\dot{\omega}$, jointly with the ω, t and $\int \omega^2 dt$ entries of the files, allows to calculate the time τ when the rotor acceleration from the previous speed was commenced:

$$\tau_i = \left(\left(\int \omega^2 dt \right)_i - \left(\int \omega^2 dt \right)_{i-1} + {\omega_{i-1}}^2 t_{i-1} - {\omega_i}^2 t_i - {\omega_{i-1}}^2 t_{a,i} + \omega_{i-1} \dot{\omega} {t_{a,i}}^2 + \frac{1}{3} \dot{\omega}^2 {t_{a,i}}^3 \right) \left({\omega_{i-1}}^2 - {\omega_i}^2 \right)^{-1} \tag{11}$$

for $\omega_i > \omega_{i-1}$, with i enumerating the scans, using the abbreviation $t_{a,i} = (\omega_i - \omega_{i-1}) / \dot{\omega}$ for the time required to change the rotor speed. A new utility function in SEDFIT was implemented to extract in this way the rotor speed history from sets of loaded scans and assemble the necessary 'speedsteps.txt' file required for the analysis.

Experimental

Model proteins were purchased from Amersham Biosciences Corp (Piscataway, NJ, kits 17-0441-01 and 17-0442-01). Lyophylized proteins were diluted into phosphate buffered saline and dialyzed overnight. DNA-coated gold nanoparticles were prepared as described (27), and streptavidin coated 15 nm gold nanoparticles were from Ted Pella, Inc. (Redding, CA), both diluted into Tris(hydroxymethyl)aminomethane (Tris) buffered saline. It should be noted that the nanoparticle samples used were stressed from extended storage past their stable lifetime, the resulting polydispersity presenting no detriment to their use as rapidly sedimenting particles in the present study. 400 μL sample volumes were matched with reference buffer and placed in charcoal-filled Epon (epoxy resin) double-sector centerpieces.

Analytical ultracentrifugation experiments were carried out in instruments using external temperature and radius calibrations (17, 28), and following the standard sedimentation velocity protocol (26) except for the following modifications. After thorough temperature equilibrium of the samples and the resting rotor in the evacuated rotor chamber, scans with standard SV settings of 0.003 cm intervals and single acquisition per radius in velocity mode were initiated through the sedimentation equilibrium method. This engages the automatic scheduler for scans and rotor speed changes.

The experimental rotor speed schedule was specified in ‘speedsteps.txt’ files introduced previously (13), containing a table of elapsed times when rotor speed changes were initiated, the new target rotor speed, and the rotor acceleration (usually 58 rad·s^{-2} (280 rpm/sec)). For data analysis, this file will be automatically recognized by SEDFIT when it is located in the scan data folder, if scans acquired at different rotor speeds are loaded. Prior to the experiment, this file can be created as an ASCII text file, and utility functions in SEDFIT can create a scanning schedule readable by the Beckman Optima XLA/I analytical ultracentrifuge operating system using the ‘equilibrium mode’ to establish precise experimental timing. Dependent on the scan parameters, different numbers of scans may be taken. This number has to be adjusted for each step such as not to cause delays between scheduled speed steps.

Results

First we were interested in examining properties of different centrifugal field schedules and their impact on the sedimentation coefficient range. To this end we considered Eq. (2) and determined the *s*-value of non-diffusing particles initially at the meniscus that would transition 1 mm into the solution column, and those that migrate out of the observation window assuming the radial range to be from 6.1 cm to 7.1 cm of a 12 mm solution column in double sector centerpieces. This will reflect the boundary position of particles with the smallest and largest *s*-value that can just be observed at any given point in time. We calculated these extreme *s*-values as a function of time for a 10 hour SV experiment for different rotor speed schedules (**Figure 1**). Essentially due to geometrical constraints, at any given time, approximately a factor of 10 in *s*-value range can be sampled in the observation window at once.

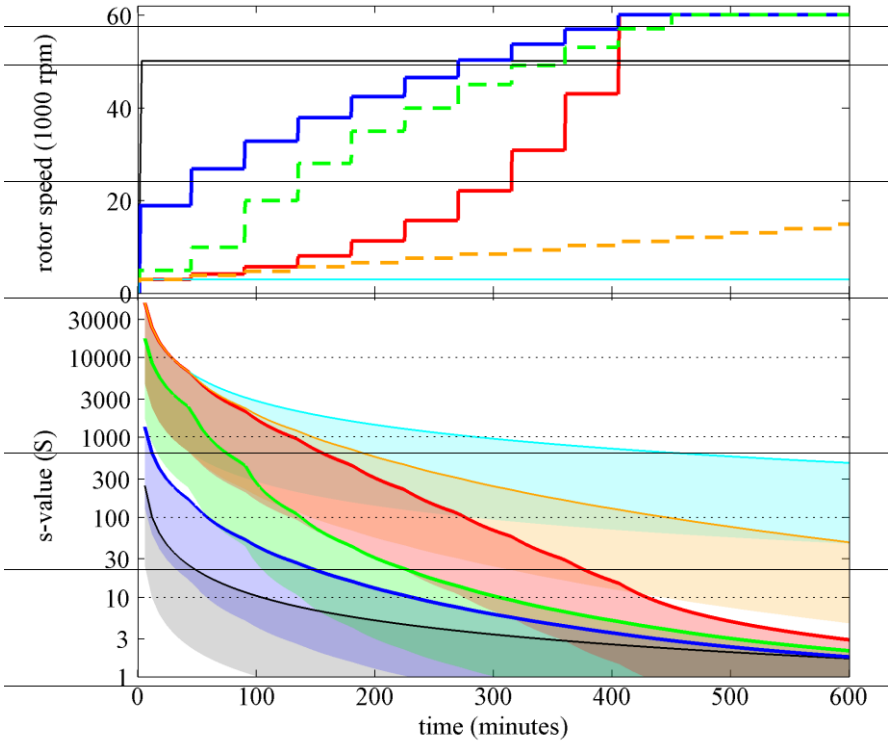

Figure 1: Range of observable sedimentation coefficients as a function of time for different rotor speed schedules. (Top) Rotor speed models following a constant field increase model (blue), a power-law model (red), an *ad hoc* model consisting of two lower speed steps at 524 rad·s^{-1} (5,000 rpm) and 1048 rad·s^{-1} (10,000 rpm) followed by a constant field increase (green dashed), and a model with slowly linearly increasing rotor speed (orange dashed). Rotor speed changes were initiated in 45 min intervals, with rotor acceleration of 29.4 rad·s^{-2} (280 rpm/sec), with ω_{low} = 314 rad·s^{-1} (3,000 rpm) and ω_{max} = 6282 rad·s^{-1} (60,000 rpm). For comparison, constant speed data are shown for a conventional constant speed experiment at 5234 rad·s^{-1} (50,000 rpm) (black) and 314 rad·s^{-1} (3,000 rpm) (cyan). (Bottom) Observable range of *s*-values for non-diffusing particles located between 6.1 cm and 7.1 cm in a 12 mm column, indicated with patches colored corresponding to the rotor speed schedules on the top.

As a reference **Figure 1** shows the conventional constant rotor speed (except for the unavoidable acceleration phase) result. At a relatively high rotor speed of 5234 rad·s^{-1} (50,000 rpm) (black line/patch) the fast particles will be observable only for a very short time, severely constraining the opportunity for their reliable detection and characterization. Within the existing initial delay for the onset of scanning (caused by delay calibrations and/or requirement for optical adjustments) in the order of minutes of a few minutes, this allows maximally particles of a few hundred 10^{-13} s (S) to be observed. With the lowest limit for detectable sedimentation coefficients being on the order of 10^{-14} s (0.1 S), the standard experiment spans approximately 3 decades of *s*-values. On the other extreme, if a very low rotor speed of 314 rad·s^{-1} (3,000 rpm) is used in a conventional constant-field experiment (cyan), very large *s*-values on the order of 10^{-9} s (10,000 S) and higher can be detected (29) but the lower limit is on the order of 10^{-11} s (100 S).

The rotor speed model designed to maximize the range is the power-law model Eq. (8), shown in red. As it starts at the lowest rotor speed and ends at the highest rotor speed it can combine the range of the low- and high-speed experiments above, spanning approximately 5 orders of magnitude. While this is ideal for extremely broadly distributed particle sizes, a disadvantage appears when a strong interest is the smallest particles of typical macromolecular size 10^{-13} s to 10^{-11} s (1 S to 100 S) or average protein size 10^{-13} s to 10^{-12} s (1 S to 10 S), because it takes several hours before the centrifugal field grows strong enough to cause their sedimentation. Another rational choice was outlined in the constant field increase model Eq. (9) (blue). Due to the initially lower fields it can achieve an approximately a 10-fold larger maximal *s*-value, while decaying continuously to the conventional high-speed model. This would satisfy a focus on intermediate particles, macromolecular assemblies and protein-sized particles. However, it would seem to sacrifice detection of the extremely large particles. Conversely, a slow linear rotor speed increase (orange) will improve the range for the large particles, but still sacrifice detection of small particles. An intermediate model consisting of a constant field increase preceded by two low-speed steps (green) appears a compromise, capturing migration of very large particles but at the same time homing in much faster on the medium/small sizes than the power-law.

A second question when attempting to model the entire sedimentation/diffusion process is how the sedimentation profiles will be shaped in gravitational sweep SV. As an example, we imposed the compromise field schedule combining the low-speed steps with a constant field increase, as shown in green in **Figure 1**, in a simulation of the sedimentation process for single species across a 10,000-fold range of molecular sizes. **Figure 2** shows the simulated concentration distributions for representative species, in a superposition of 100 scans in equally spaced 5 min intervals for the duration of 8.5 hours. The same color temperature scheme is used for all to indicate later times with higher temperature, with green being centered at ≈ 4 hours. In some plots, different rotor speed steps may be discerned from regions of different line

density, which reflects the rate of boundary migration in the current field. The most striking feature of **Figure 2** is how the boundaries from different size species 'peel off' the meniscus and migrate into the cell at their characteristic time while they will remain spatially well-separated. A salient feature of the direct boundary modeling is that data from the entire time-course can be modeled at once, and this will allow the natural combination of information from particles of all sizes.

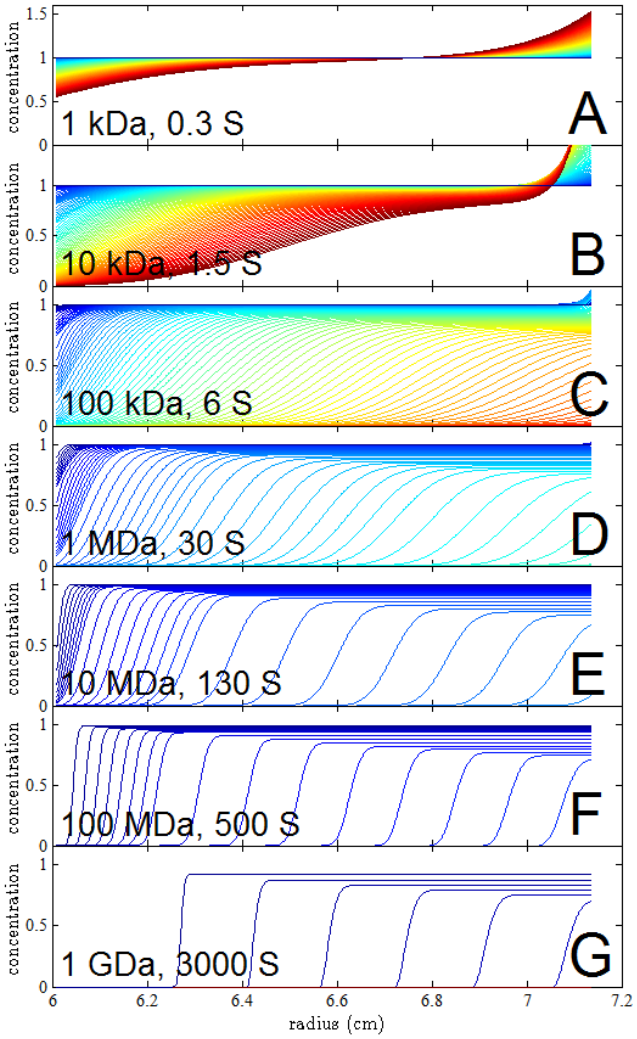

Figure 2: Calculated boundary profiles of discrete species sedimenting in variable field SV under conditions of the schedule shown in green in Figure 1. Radial concentration profiles are calculated for a time-period from ≈ 9 min to 8.5 hours, in 100 scans of 5 min intervals. All panels show the radial profiles using the same color scheme with increasing color temperature indicating later time. For reference, the green range is approximately in the middle of the experiment where the rotor speed is 4188 rad·s^{-1} (40,000 rpm). Sedimentation was simulated for particles with partial-specific volume of 0.73 ml/g in water, with frictional ratios between 1.2 to 1.5. Sedimentation parameters are for species of (A) 10^3 g·mol^{-1} (1 kDa), 0.3 × 10^{-13} s (0.3 S); (B) 10^4 g·mol^{-1} (10 kDa), 1.5 × 10^{-13} s (1.5 S); (C) 10^5 g·mol^{-1} (100 kDa), 6 × 10^{-13} s (6 S); (D) 10^6 g·mol^{-1} (1 MDa), 30 × 10^{-13} s (30 S); (E) 10^7 g·mol^{-1} (10 MDa), 130 × 10^{-13} s (130 S); (F) 10^8 g·mol^{-1} (100 MDa), 500 × 10^{-13} s (500 S); (G) 10^9 g·mol^{-1} (1 GDa), 3000 × 10^{-13} s (3,000 S).

Another interesting aspect of the sedimentation boundary shapes is that all exhibit significant boundary broadening with time, despite their very dissimilar diffusion coefficients. This is clearly due to the different time scales involved in their sedimentation process, where large particles are observed at low speed, such that the rate of diffusional transport remains large relative to sedimentation. In fact, even for moderate and small particles, boundary broadening is exacerbated by the slow migration at the earlier times at lower fields. To quantify this, we considered the data from Panel C (simulated for a 10^5 g·mol^{-1} (100 kDa) protein with 6×10^{-13} s (6 S)) during to the 4188 rad·s^{-1} (40,000 rpm) step, which comprises scans 45 to 53 that show in green the boundary midpoint between 6.3 cm and 6.45 cm. When we subjected this data set to a simplistic Lamm equation analysis on the basis of 'effective sedimentation times' Eq. (3), the best-fit sedimentation coefficient is 5.95×10^{-13} s (5.95 S), as expected very close to the value of 6×10^{-13} s (6 S) underlying the simulation. However, the best-fit molar mass is only 57×10^3 g·mol^{-1} (57 kDa) rather than the 10^5 g·mol^{-1} (100 kDa) underlying the gravitational sweep SV simulation. This discrepancy is caused by increased diffusion time during the prolonged low speed phases of the experiment, which is not accounted for in the approximation of 'effective sedimentation times' Eq. (3). Thus, the analysis of variable field SV profiles cannot be carried out without full consideration of the true centrifugal field schedule.

On the other hand, the question arises whether diffusional boundary broadening for very large particles can be distinguished from polydispersity. For example, the data from Figure 2G (with $3\,000 \times 10^{-13}$ s (3,000 S)) can be fit well with a distribution of non-diffusing particles (with a square root of the second moment of 60×10^{-13} s (60 S)) producing a root mean-square deviation (rmsd) of only 0.32 % (with maximum error < 6 %) of the loading signal. This is below the signal/noise level of typical data acquisition, and therefore would be indistinguishable. By contrast, the data from the 500 S particle in Figure 2F cannot be fit well with a distribution of non-diffusing particles, producing an rmsd of 2 % (with maximum error > 25 %) of the loading signal, and even less so the 130×10^{-13} s (130 S) data of Figure 2E, which produce an rmsd of 3.2 % (with maximum error > 30 %) of the loading signal. For these smaller particles, therefore, the presence of diffusion contributions should be discernable even for particles with continuous size distributions.

Finally we tested the experimental application of gravitational sweep SV. For the implementation of a rotor speed schedule the accurate timing of rotor speed changes is important. It is generally preferable to avoid manual adjustments, by taking advantage of the pre-programmed rotor speed changes in the 'sedimentation equilibrium method' data acquisition mode of the graphical user interface of the Beckman Coulter analytical ultracentrifuge. The main character of this data acquisition mode is that it can execute serially

sedimentation steps at different rotor speeds and temperature, and initiate scans at each step at pre-set time intervals. Although the rules for the precise timing of speed changes and scans are non-obvious, in the previous communication on variable-field AUC (13) we have reported on a new utility function in SEDFIT that can convert between 'speedsteps.txt' files and 'sedimentation equilibrium method' .equ files that can be loaded into the analytical ultracentrifuge user interface (see tutorial video https://sedfitsedphat.nibib.nih.gov/tools/Protocols/TOSE_implementation.wmv). However, for the desired timing to be honored it is important that the total time for the sequence of scans at each step – including delay calibration – does not exceed the allotted total time for the rotor to reside at the current speed; otherwise speed changes will be delayed. This requires a conservative estimate for the scan time, which depends on radial resolution, number of replicates, scanning mode, number of cells, and rotor speed at low speeds. It can be determined prior to the gravitational sweep SV experiment. For example, at rotor speeds above 522 rad·s^{-1} (5,000 rpm) an estimate at standard SV scan settings of 0.003 cm target radial interval with a single acquisition in velocity mode in our instruments is ≈ 2 min for the first scan (requiring delay calibration) and ≈ 1 min for the following scans per cell.

Fortunately, it is also possible to retroactively extract the rotor speed schedule from experimental data files *via* Eq. (11) provided each rotor speed is represented by at least a single scan. When applied to experimental data preprogrammed for the green schedule in **Figure 1**, the reconstructed time points of rotor speed changes were consistent with the preprogrammed time-points within 0.5 % or better. With time-stamp errors accounted for (16), the source of the remaining small discrepancy is unclear, but the magnitude is within the typical relative accuracy of *s*-values (28). Thus, this approach provides a useful fallback for inconsistent preprogrammed schedules, or when speed schedules are adjusted *ad hoc* in real-time.

Prior to data analysis, pre-processing of scans is essential to eliminate the translation of the solution column due to rotor stretching *via* Eq. (7). At this stage, residual scan time errors can also be removed (16, 17). A very sensitive measure for radial alignment is the successful elimination of time-invariant residual features across all scans, as visualized by the absence of vertical features from the residuals bitmap after fit. This worked well using the pre-determined stretching modulus (30) as implemented in SEDFIT. Some residual small shifts at low rotor speed remained (see **Figure 3** below, and **Supplementary Material Figure 1**), possibly reflecting rotor-speed dependent shifts in the axis of rotation not accounted for in Eq. (7). Such shifts were examined for the Model E ultracentrifuge and found to affect translation of the solution column approximately tenfold less than the effect of rotor stretching (31, 32).

Figure 3 shows the absorbance profiles in a gravitational sweep SV experiment of a mixture of samples of chymotrypsinogen A sedimenting at 2.5 × 10^{-13} s (2.5 S), catalase at 10.8 × 10^{-13} s (10.8 S), thyroglobulin

at 18.8 × 10^{-13} s (18.8 S) with oligomers in the 25 × 10^{-13} s to 40 × 10^{-13} s (25 S to 40 S) range, and ferritin, the latter exhibiting a broad distribution with weighted average *s*-value of 68 S in addition to oligomers and aggregates spanning up to 200 × 10^{-13} s (200 S). For the centrifugal field profile the extended constant field increase model shown in green in **Figure 1A** was used. A clear separation of the boundaries for all proteins can be discerned. Each protein sample was inserted into the mixture at equal final concentrations of ~ 0.2 g·L^{-1} (0.25 OD_{280}/1.2cm), which corresponds well to the observed boundary heights. In control experiments at 2094 rad·s^{-1} (20,000 rpm) and 5234 rad·s^{-1} (50,000 rpm) constant speed, as expected, no simultaneous observation of the largest and smallest species was possible (data not shown).

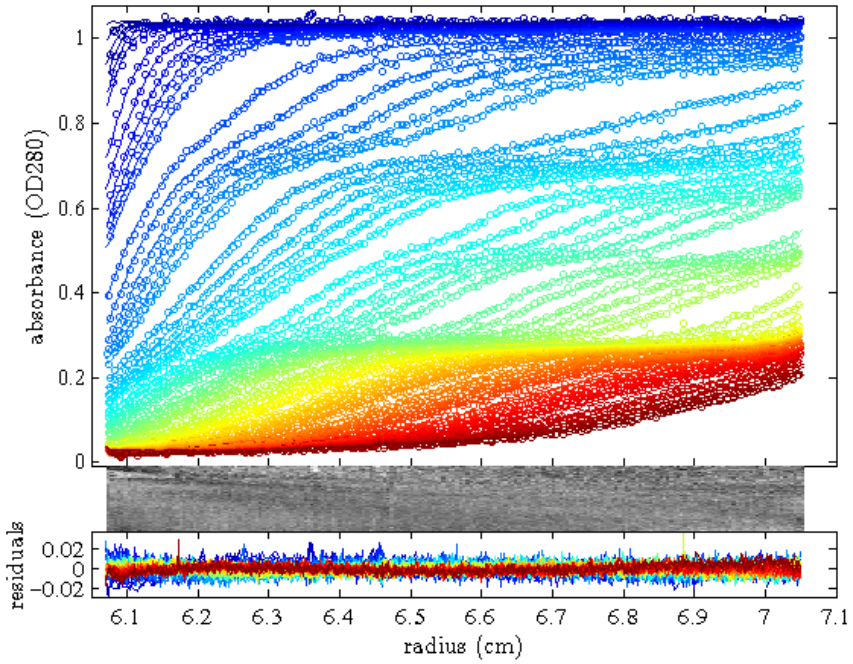

Figure 3: Variable-field SV experiment using a mixture of 4 proteins (chymotrypsinogen A, catalase, thyroglobulin, and ferritin) subjected to the extended power-law rotor speed schedule shown in green in Fig. 1**.** Top: Circles are experimental data points (only every 3rd shown) in 66 scans acquired from 8 min to 489 min in ≈ 6 min intervals, and approximately twice this delay after acceleration phases, which can be recognized from the apparent gaps in scan pattern. The line is the best-fit *c*(*s*) distribution model, as shown in Fig. 4. Middle and Bottom Panels show the bitmap and overlay of the residuals, which have a root-mean-square deviation of 0.0050 OD and a relative deviation from normal distribution (33) of H = 1.0 %.

An excellent fit could be achieved with the standard *c*(*s*) model. For covering large *s*-value ranges we applied a logarithmically spaced grid. We found it necessary to increase the P-value for regularization,

applying a stronger constraint for parsimony of the distribution than usually achieved from relying on F-statistics allowing for one or two standard deviation increase in the root-mean-square deviation (rmsd). We believe this is related to the fact that information on any given *s*-range rests only on a subset of scans, constituting a much smaller fraction of the total number of data points than in constant speed SV. As mentioned above, 'unstretching' absorbance scans allowed a good description of time-invariant (TI) noise. In some experiments we observed clear shifts in baseline associated with rotor speed changes (data not shown). This can be captured with a radial-invariant (RI) noise offset model. Therefore, although RI noise is ordinarily not required for modeling absorbance data (26), it was included for modeling variable-field SV absorbance data.

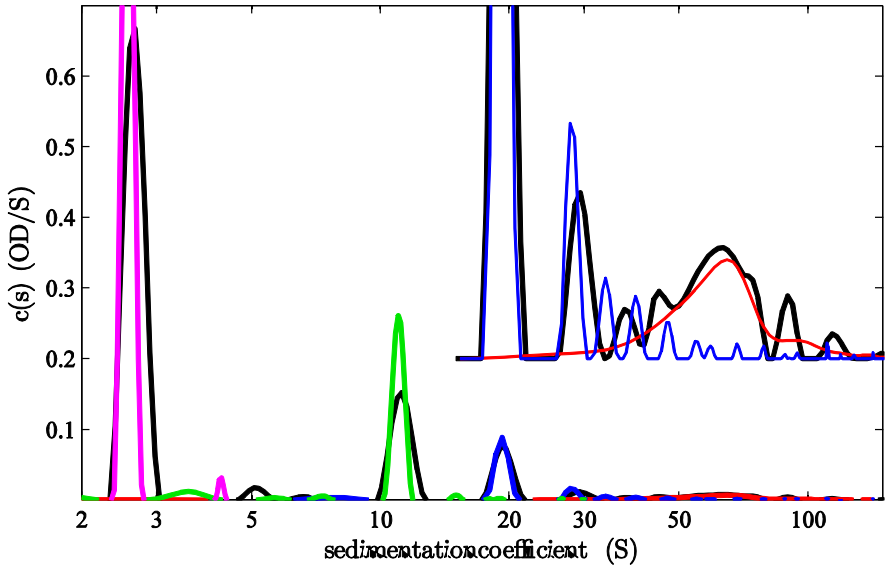

Figure 4: Sedimentation coefficient distribution *c*(*s*) corresponding to the fit of the variable-field SV experiment shown in Fig. 3 (black line). In order to better visualize the distribution at larger *s*-values, it was repeated with 20-fold amplification and offset by 0.2 OD. For comparison with the variable-field experiment (black), also shown are the distributions of chymotrypsinogen A (magenta) and catalase (green) obtained in a conventional constant-speed SV experiment at 5234 rad·s^{-1} (50,000 rpm), and the distributions of thyroglobulin (blue) and ferritin (red) obtained in a constant-speed SV experiment at 2094 rad·s^{-1} (20,000 rpm).

The resulting *c*(*s*) distribution is shown as bold in **Figure 4** (bold black line). We compared the distribution with *c*(*s*) distributions obtained from conventional constant-speed SV experiments of the individual samples conducted at 2094 rad·s^{-1} (20,000 rpm) (ferritin and thyroglobulin) and 5234 rad·s^{-1} (50,000 rpm) (catalase and chymotrypsinogen A). The results of the individual *c*(*s*) traces is consistent with the gravitational sweep results. Lower resolution appears to be achieved in the gravitational speed experiment for the

oligomers of thyroglobulin where trace dimer and trimer seems to be merged, but ferritin oligomers could be better resolved in the gravitational sweep.

Finally, in order to explore further the dynamic range of gravitational sweep SV, we carried out experiments with samples expected to have even higher *s*-values: A sample of DNA-coated gold nanoparticles with modal *s*-values of ≈ 350 × 10^{-13} s (350 S) (**Supplementary Information Figure S1**), and samples of streptavidin-coated gold nanoparticles with a modal *s*-value of ≈ 950 × 10^{-13} s (950 S) (**Supplementary Information Figure S2**) could both be resolved using the same 'extended constant field increase' speed schedule as applied for the protein mixture. Interestingly, in the latter sample a small 2.6 × 10^{-13} s (2.6 S) species – consistent with the expected size of free streptavidin – could be resolved cosedimenting with the nanoparticles ranging in sedimentation coefficient up to a few thousand 10^{-13} s (Svedbergs).

Discussion

Previous approaches (4, 6) of gravitational sweep or multi-speed SV were successful in demonstrating the detection of large particles over a very wide range of sizes, but the lack of consideration of diffusion limited the size resolution that could potentially be achieved, as well as the smallest particle sizes that could be distinguished. This problem is exacerbated in the variation of the 'wide distribution analysis' (6), where the time-derivative method to calculate an apparent sedimentation coefficient distribution $g(s^*)$ (15) is subject to additional artificial broadening from the discrete approximation of dc/dt even for very large, non-diffusing particles (23), which restricts the choice of rotor speeds and number of scans that can be included into such an analysis.

In the present work, we have addressed these limitations by solving the Lamm equation for the coupled sedimentation/diffusion process in a time-varying centrifugal field, to be used as kernel in diffusion-deconvoluted sedimentation coefficient distributions $c(s)$ (14) or size-and-shape distributions (20). This approach inherits the lower size-limit of detectable sedimentation in Lamm equation modeling, along with the exquisite hydrodynamic resolution of $c(s)$ – for example, routinely providing baseline-separation of monomers and dimers of small proteins – and all the advantages in data range, statistical accuracy, noise analysis, and quality control of direct boundary modeling in the raw data space. Although we have experimentally demonstrated only a ~ 1,000-fold range of sedimentation coefficients, the considerations in the present work suggest that particles across the entire spectrum of size ranges detectable by SV should be accessible in a single gravitational sweep experiment: with sedimentation coefficients ranging from 0.1×10^{-13} s (0.1 S) to 10000×10^{-13} s (10,000 S), this comprises eight orders of magnitude in mass, starting at the smallest detectable species such as buffer salts and small molecules on the order of 10^2 Da sedimenting at the high rotor speeds (34, 35), up to entire organisms in the 10^{10} Da range sedimenting ahead already at the lowest rotor speeds (29).

In order to apply the $c(s)$ analysis to gravitational sweep SV data, some prior knowledge about an approximate relationship between sedimentation and diffusion is useful. In standard SV this is often accomplished with a scaling law for compact particles, with an average frictional ratio as an adjustable parameter (14, 19), although a few other, and more general scaling models are currently implemented in SEDFIT (36). Dependent on the sample, not all detectable particles in gravitational sweep SV may follow the same scaling law. This may be addressed, with the multi-modal models, or tabulated relationships, or with future extensions as needed for the study of particular samples. However, it should be noted that the significance of diffusion – and therefore the required precision for approximate description – will decrease with increasing particle size. Our experience so far suggests that this is not critical as long as the focus remains on the sedimentation coefficient distribution, as opposed to molar mass distributions, which will

be far less reliable, particularly for large particles. Size-and-shape distributions expressed as $c(s,D)$ will completely circumvent this problem, especially when the ill-defined diffusion dimension is collapsed to the general $c(s,*)$ (20).

The new method has virtually no restrictions in shape and number of scans that can be included, and virtually no restrictions in the selection of rotor speed profiles. This offers a great freedom of experimental design. We have explored several centrifugal field schedules, which may be chosen dependent on the system under study. Since an extended dynamic range comes at the price of reduced information content on a particular species, as compared to a conventional SV experiment at suitably chosen constant speed, we do not anticipate gravitational sweep SV to become the method of choice when species of interest are known to fall within a narrow *s*-range (e.g., within a factor 10). Even though a 100-fold or larger range of *s*-values is easily detectable during the course of a constant speed experiment, faster particles migrate rapidly through the solution column and are therefore observed only for a short time. The application of field schedules with constant rate of rotor speed increase (for large particles) or constant rate of field increase (for small particles), permit a ~100-fold range of *s*-values to be explored more thoroughly. The widest range possible with uniform resolution can be achieved with a power law model. However, deviations from these models are easily possible, such as the 'extended constant field increase' model used for the experiments in the present study; it has a wide range but focuses more on the smaller sizes. There is virtually complete freedom; a much simpler application enhancing standard SV could consist, for example, in a single moderate speed step at 2094 $rad \cdot s^{-1}$ (20,000 rpm) for the duration of an hour – to better capture possible large aggregates – followed by the standard high-speed condition at 5234 $rad \cdot s^{-1}$ (50,000 rpm) for the remaining time to sediment medium and small proteins.

The time-varying centrifugal fields can be implemented either in a pre-programmed mode, or be adjusted *ad hoc*, with the limitation that at least one scan must report on each speed step to allow reconstruction of the field variation. Similar to potential rotor speed adjustments in SE, it is conceivable that real-time $c(s)$ analysis (which might show, for example, the apparent lack of particles migrating at the momentary speed) could automatically lead to decisions to increase rotor speeds, creating a dynamic feed-back for optimal analysis of unknown samples. Unfortunately, this is not possible with current instrumentation due to the absence of accessible speed and scan control interfaces in the centrifugal operating software.

Besides enabling gravitational sweep analysis, the variable field extension of SV has implications for how conventional experiments can be conducted. First, it appears sometimes desirable to use an initial single low-speed step, typically at 314 $rad \cdot s^{-1}$ (3,000 rpm), to allow time for leak tests and optical adjustments. This can now be naturally accounted for in the framework of time-varying centrifugal fields, without

causing detrimental effects on the accuracy of the data analysis. With knowledge of the rotor speed and the standard acceleration, it is possible to reconstruct the exact duration of the low-speed step. Temperature equilibration, however, should still be carried out with the rotor at rest, prior to any centrifugation, in order not to cause convective disturbances of any sedimentation and diffusion processes. With respect to temperature accuracy, another side-effect of the extension of SV to time-varying centrifugal fields is the opportunity to carry out slow rotor acceleration phases in isothermal mode, avoiding adiabatic cooling during the rapid stretching of the rotor through radiative heat flow (9).

We believe gravitational sweep SV in conjunction with $c(s)$ analysis introduced in the present communication will be particularly useful in the study of proteins that self-assemble into large structures, such as virions or fibrils, which can currently not be easily characterized simultaneously with their free building blocks. Similarly, equilibria between very dissimilar sized macromolecules or particles should be better accessible without compromising the detection of either small or large reactant. Finally, a natural field of applications are broadly distributed nanoparticles (37), in biotechnology (7), and samples of entirely unknown distribution.

Author Contributions

JM designed experiments, performed research and analyzed data; JS, JAL provided materials; HZ, PS: designed experiments, analyzed data, contributed analytical tools, and wrote the paper

Acknowledgments

This work was supported by the Intramural Research Program of the National Institute of Biomedical Imaging and Bioengineering, National Institutes of Health.

References

1. Nossal, R.J., and G.H. Weiss. 1970. Sedimentation in a time-varying ultracentrifuge. Anal. Biochem. 38: 115–120.

2. Scholtan, W., and H. Lange. 1972. Bestimmung der Teilchengrößenverteilung von Latices mit der Ultrazentrifuge. Kolloid-Z. u. Z. Polym. 250: 782–796.

3. Mächtle, W. 1988. Coupling particle size distribution technique. A new ultracentrifuge technique for determination of the particle size distribution of extremely broad distributed dispersions. Angew. Makromol. Chem. : 35–52.

4. Mächtle, W. 1999. High-resolution, submicron particle size distribution analysis using gravitational-sweep sedimentation. Biophys. J. 76: 1080–1091.

5. Runge, M.S., T.M. Laue, D.A. Yphantis, M.R. Lifsics, A. Saito, et al. 1981. ATP-induced formation of an associated complex between microtubules and neurofilaments. Proc. Natl. Acad. Sci. U. S. A. 78: 1431–1435.

6. Stafford, W.F., and E.H. Braswell. 2004. Sedimentation velocity, multi-speed method for analyzing polydisperse solutions. Biophys. Chem. 108: 273–9.

7. Mach, H., and T. Arvinte. 2011. Addressing new analytical challenges in protein formulation development. Eur. J. Pharm. Biopharm. 78: 196–207.

8. Schuck, P., Z. Taraporewala, P. McPhie, and J.T. Patton. 2001. Rotavirus nonstructural protein NSP2 self-assembles into octamers that undergo ligand-induced conformational changes. J. Biol. Chem. 276: 9679–9687.

9. Zhao, H., A. Balbo, H. Metger, R. Clary, R. Ghirlando, et al. 2014. Improved measurement of the rotor temperature in analytical ultracentrifugation. Anal. Biochem. 451: 69–75.

10. Schuck, P. 1998. Sedimentation analysis of noninteracting and self-associating solutes using numerical solutions to the Lamm equation. Biophys. J. 75: 1503–1512.

11. Brown, P.H., and P. Schuck. 2008. A new adaptive grid-size algorithm for the simulation of sedimentation velocity profiles in analytical ultracentrifugation. Comput. Phys. Commun. 178: 105–120.

12. Claverie, J.M., H. Dreux, and R. Cohen. 1975. Sedimentation of generalized systems of interacting particles. I. Solution of systems of complete Lamm equations. Biopolymers. 14: 1685–1700.

13. Ma, J., M. Metrick, R. Ghirlando, H. Zhao, and P. Schuck. 2015. Variable-field analytical ultracentrifugation: I. Time-optimized sedimentation equilibrium. Biophys J. in press.

14. Schuck, P. 2000. Size-distribution analysis of macromolecules by sedimentation velocity ultracentrifugation and Lamm equation modeling. Biophys. J. 78: 1606–1619.

15. Stafford, W.F. 1992. Boundary analysis in sedimentation transport experiments: a procedure for obtaining sedimentation coefficient distributions using the time derivative of the concentration profile. Anal. Biochem. 203: 295–301.

16. Zhao, H., R. Ghirlando, G. Piszczek, U. Curth, C.A. Brautigam, et al. 2013. Recorded scan times can limit the accuracy of sedimentation coefficients in analytical ultracentrifugation. Anal. Biochem. 437: 104–108.

17. Ghirlando, R., A. Balbo, G. Piszczek, P.H. Brown, M.S. Lewis, et al. 2013. Improving the thermal, radial, and temporal accuracy of the analytical ultracentrifuge through external references. Anal. Biochem. 440: 81–95.

18. Lamm, O. 1929. Die Differentialgleichung der Ultrazentrifugierung. Ark. Mat. Astr. Fys. 21B(2): 1–4.

19. Schuck, P., M.A. Perugini, N.R. Gonzales, G.J. Howlett, and D. Schubert. 2002. Size-distribution analysis of proteins by analytical ultracentrifugation: strategies and application to model systems. Biophys. J. 82: 1096–1111.

20. Brown, P.H., and P. Schuck. 2006. Macromolecular Size-And-Shape Distributions by Sedimentation Velocity Analytical Ultracentrifugation. Biophys. J. 90: 4651–4661.

21. Schuck, P. 2010. On computational approaches for size-and-shape distributions from sedimentation velocity analytical ultracentrifugation. Eur. Biophys. J. 39: 1261–1275.

22. Brown, P.H., A. Balbo, and P. Schuck. 2007. Using prior knowledge in the determination of macromolecular size-distributions by analytical ultracentrifugation. Biomacromolecules. 8: 2011–2024.

23. Schuck, P., and P. Rossmanith. 2000. Determination of the sedimentation coefficient distribution by least-squares boundary modeling. Biopolymers. 54: 328–341.

24. Schuck, P. 2010. Some statistical properties of differencing schemes for baseline correction of sedimentation velocity data. Anal. Biochem. 401: 280–287.

25. Schuck, P., and B. Demeler. 1999. Direct sedimentation analysis of interference optical data in analytical ultracentrifugation. Biophys. J. 76: 2288–2296.

26. Zhao, H., C.A. Brautigam, R. Ghirlando, and P. Schuck. 2013. Current methods in sedimentation velocity and sedimentation equilibrium analytical ultracentrifugation. Curr. Protoc. Protein Sci. 7: 20.12.1.

27. Ko, S.H., F. Vargas-Lara, P.N. Patrone, S.M. Stavis, F.W. Starr, et al. 2014. High-speed, high-purity separation of gold nanoparticle-DNA origami constructs using centrifugation. Soft Matter. 10: 7370–7378.

28. Zhao, H., R. Ghirlando, C. Alfonso, F. Arisaka, I. Attali, et al. 2015. A multilaboratory comparison of calibration accuracy and the performance of external references in analytical ultracentrifugation. PLoS One. 10: e0126420.

29. Trachtenberg, S., P. Schuck, T.M. Phillips, S.B. Andrews, and R.D. Leapman. 2014. A structural framework for a near-minimal form of life: Mass and compositional analysis of the helical mollicute Spiroplasma melliferum BC3. PLoS One. 9: e87921.

30. Brown, P.H., A. Balbo, and P. Schuck. 2009. On the analysis of sedimentation velocity in the study of protein complexes. Eur. Biophys. J. 38: 1079–1099.

31. Baghurst, P.A., and P.E. Stanley. 1970. Determination of stretch of a titanium analytical ultracentrifuge rotor subjected to various centrifugal fields. Anal. Biochem. 33: 168–173.

32. Schachman, H.K. 1959. Ultracentrifugation in Biochemistry. New York: Academic Press.

33. Ma, J., H. Zhao, and P. Schuck. 2015. A histogram approach to the quality of fit in sedimentation velocity analyses. Anal. Biochem. 483: 1–3.

34. Zhao, H., P.H. Brown, A. Balbo, M.C. Fernandez Alonso, N. Polishchuck, et al. 2010. Accounting for solvent signal offsets in the analysis of interferometric sedimentation velocity data. Macromol. Biosci. 10: 736–745.

35. Pavlov, G.M., E.V. Korneeva, N.A. Smolina, and U.S. Schubert. 2010. Hydrodynamic properties of cyclodextrin molecules in dilute solutions. Eur. Biophys. J. 39: 371–379.

36. Harding, S.E., P. Schuck, A.S. Abdelhameed, G. Adams, M.S. Kök, et al. 2011. Extended Fujita approach to the molecular weight distribution of polysaccharides and other polymeric systems. Methods. 54: 136–44.

37. Walter, J., P.J. Sherwood, W. Lin, D. Segets, W.F. Stafford, et al. 2015. Simultaneous analysis of hydrodynamic and optical properties using analytical ultracentrifugation equipped with multiwavelength detection. Anal. Chem. 87: 3396–3403.

Supplementary Material

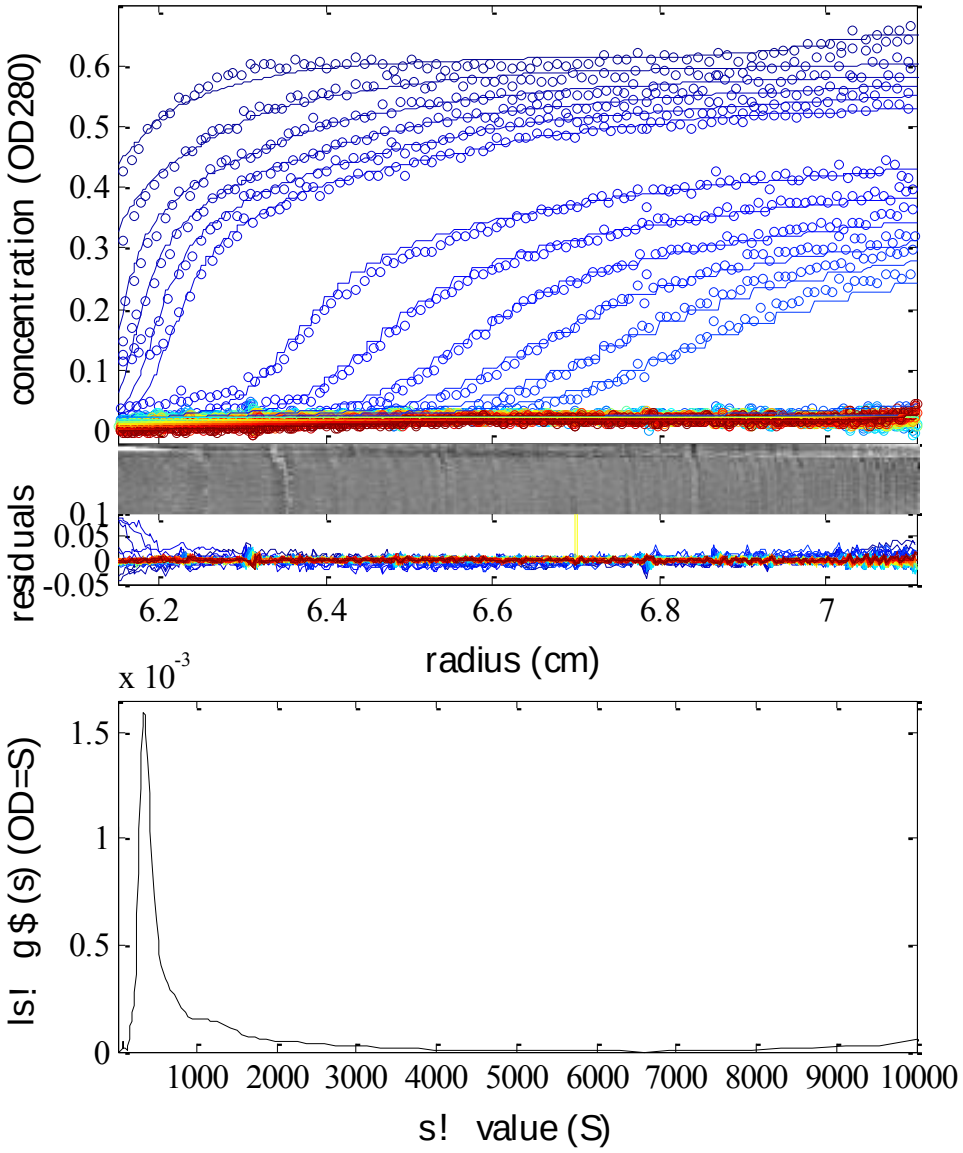

Figure S1: Sedimentation coefficient distribution ls-g*(s) of a preparation of DNA-coated Au nanoparticles diluted in TRIS buffered saline. Top: Absorbance data at 280 nm (circles, only every 3rd data point shown) were acquired in a gravitational sweep experiment using the same 'extended constant field increase' rotor speed schedule shown in green in Figure 1, identical to the centrifugal field sequence used in the protein mixture experiments shown in Figure 3. The analysis of the data was carried out with a ls-g*(s) model for a broad distribution of non-diffusing particles, superimposed with a single diffusing species with apparent s-value of 1.02×10^{-13} s (1.02 S) and 12×10^{3} g·mol^{-1} (12 kDa) (based on a partial specific volume scale of 0.73 ml/g in normal solvent conditions at 20 °C). The best-fit model is shown as solid lines. Middle: residuals in overlay and bitmap format, leading to an rmsd of 0.0066 OD.

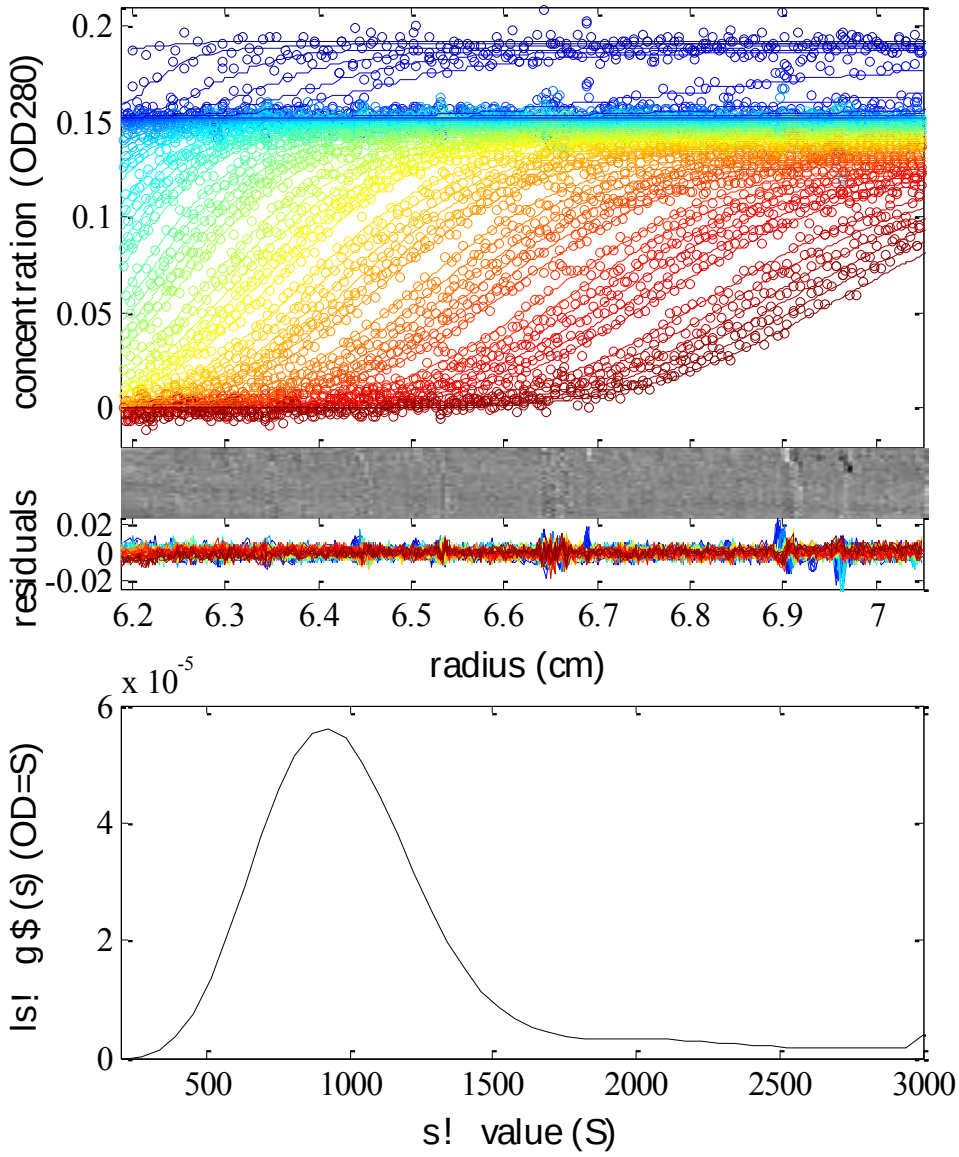

Figure S2: Sedimentation coefficient distribution ls-g*(s) of an aged preparation of streptavidin-coated 15 nm Au nanoparticles diluted in TRIS buffered saline. Top: Absorbance data at 280 nm (circles, only every 3rd data point shown) were acquired in a gravitational sweep experiment using the same 'extended constant field increase' rotor speed schedule shown in green in Figure 1, identical to the centrifugal field sequence used in the protein mixture experiments shown in Figure 3. The analysis of the data was carried out with a ls-g*(s) model for a broad distribution of non-diffusing particles, superimposed with a single diffusing species with apparent s-value of 2.6×10^{-13} s (2.6 S) and 40×10^{3} g·mol^{-1} (40 kDa) (based on a partial specific volume scale of 0.73 ml/g in normal solvent conditions at 20 °C). The best-fit model is shown as solid lines. Middle: residuals in overlay and bitmap format, leading to an rmsd of 0.0034 OD.